



UNIVERSITY OF LEEDS

This is a repository copy of *Application of particle image velocimetry measurement techniques to study turbulence characteristics of oscillatory flows around parallel-plate structures in thermoacoustic devices*.

White Rose Research Online URL for this paper:  
<http://eprints.whiterose.ac.uk/79740/>

Version: Accepted Version

---

**Article:**

Mao, X and Jaworski, AJ (2010) Application of particle image velocimetry measurement techniques to study turbulence characteristics of oscillatory flows around parallel-plate structures in thermoacoustic devices. *Measurement Science and Technology*, 21 (3). 3. 035403 - 035403. ISSN 0957-0233

<https://doi.org/10.1088/0957-0233/21/3/035403>

---

**Reuse**

Unless indicated otherwise, fulltext items are protected by copyright with all rights reserved. The copyright exception in section 29 of the Copyright, Designs and Patents Act 1988 allows the making of a single copy solely for the purpose of non-commercial research or private study within the limits of fair dealing. The publisher or other rights-holder may allow further reproduction and re-use of this version - refer to the White Rose Research Online record for this item. Where records identify the publisher as the copyright holder, users can verify any specific terms of use on the publisher's website.

**Takedown**

If you consider content in White Rose Research Online to be in breach of UK law, please notify us by emailing [eprints@whiterose.ac.uk](mailto:eprints@whiterose.ac.uk) including the URL of the record and the reason for the withdrawal request.



[eprints@whiterose.ac.uk](mailto:eprints@whiterose.ac.uk)  
<https://eprints.whiterose.ac.uk/>

# Application of particle image velocimetry measurement techniques to study turbulence characteristics of oscillatory flows around parallel-plate structures in thermoacoustic devices

Xiaoan MAO and Artur J. JAWORSKI \*

School of Mechanical, Aerospace and Civil Engineering, University of Manchester, Sackville Street, PO Box 88,  
Manchester M60 1QD, United Kingdom

\* Corresponding author: [a.jaworski@manchester.ac.uk](mailto:a.jaworski@manchester.ac.uk), T: +44(0)161 275 4352, F: +44(0)870 130 7474

## Abstract

This paper describes the development of the experimental setup and measurement methodologies to study the physics of oscillatory flows in the vicinity of parallel plate stacks by using the particle image velocimetry (PIV) techniques. Parallel plate configurations often appear as internal structures in thermoacoustic devices and are responsible for the hydrodynamic energy transfer processes. The flow around selected stack configurations is induced by a standing acoustic wave, whose amplitude can be varied. Depending on the direction of the flow within the acoustic cycle, relative to the stack, it can be treated as an entrance flow or a wake flow. The insight into the flow behaviour, its kinematics, dynamics and scales of turbulence, is obtained using the classical Reynolds decomposition to separate the instantaneous velocity fields into ensemble-averaged mean velocity fields and fluctuations in a set of predetermined phases within an oscillation cycle. The mean velocity field and the fluctuation intensity distributions are investigated over the acoustic oscillation cycle. The velocity fluctuation is further divided into large- and small-scale fluctuation by using Fast Fourier Transform (FFT) spatial filtering techniques.

Keywords: oscillatory flow, parallel plate structure, thermoacoustics, turbulence and coherence, spatial filtering

## 1 Introduction

In thermoacoustic devices, an acoustic wave interacts with a stack of tightly spaced plates either to produce acoustic power, induced by a temperature gradient on the stack, or to obtain a temperature gradient along the stack, induced by an imposed acoustic wave. This is based on the thermoacoustic effect whereby appropriately phased pressure and velocity oscillations enable the compressible fluid to undergo a thermodynamic cycle in the vicinity of a solid body. These processes have been utilised in thermoacoustic engines and coolers [1], whose main advantages are their lack of moving parts and construction simplicity: the conversion between thermal and acoustic energies is realised by an oscillating gas, without the need for piston-cylinder arrangements, sliding seals or harmful working fluids.

Figure 1 shows a schematic of a quarter-wavelength, standing wave device working as a refrigerator thanks to the acoustic power input,  $W_{ac}$ . Central to the device's operation is a thermoacoustic stack. This can be imagined as a

series of plates forming a set of parallel channels. The gas pressure in the resonator oscillates acoustically at a frequency set by the resonance between the gas in the duct and the moving mass of the transducer. The distributions of pressure amplitude,  $|p|$  and velocity amplitude,  $|u|$  illustrate the standing wave present in the resonator. The oscillating gas, within a short distance of thermal penetration depth,  $\delta_v$  from the adjacent solid boundaries, communicates heat with the stack (as shown on the right) and heat exchangers, and the acoustics of the system ensure that the timing between the pressure and gas displacement is such that heat (the cooling load,  $Q_c$ ) is pumped out of the cold heat exchanger towards the hot heat exchanger (and removed to the surroundings as denoted by  $Q_h$ ), using a hydrodynamic energy transfer “cascade” enabled by compressing and expanding gas parcels. It is also possible to reverse the operation of such systems to form an engine: a high temperature gradient along the stack leads to a spontaneous generation of acoustic power which can be converted to electricity by a linear alternator. More complex systems can be built utilising the concept of “travelling wave” devices [2] which are not discussed here for simplicity.

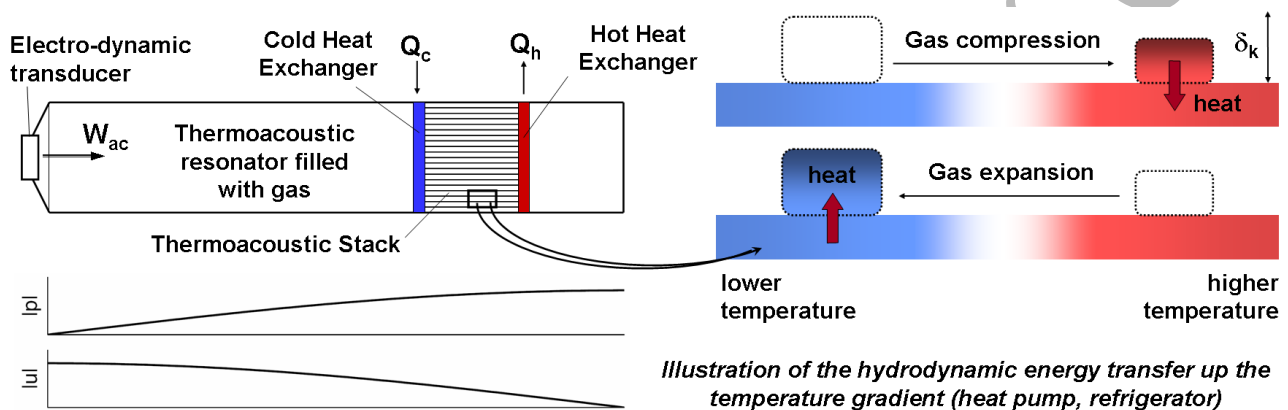


**Figure 1 Schematic of a simple thermoacoustic cooler arrangement. The acoustically induced compression and expansion of fluid elements causes heat pumping effects along the stack.**

The intensity of acoustic waves used in thermoacoustic applications is usually described by their “drive ratio”: the ratio of the maximum pressure amplitude of the acoustic wave to the mean pressure in the resonator ( $Dr$ ). It is thought that up to drive ratios of about 2-3 % the fluid flow and heat transfer processes can be reliably described by the linear acoustic theory developed by Rott [3]. However, practical applications often require drive ratios as high as 10 %, in which range the interaction between the acoustic field and the solid boundary is governed by complex thermal-fluid processes, which are still not fully understood. Large drive ratios correspond to large fluid displacements and velocity amplitudes, which in turn lead to significant nonlinear effects such as local pressure losses caused by the abrupt change of the cross section, acoustic streaming, vortex shedding and transition to turbulence. These factors can have a significant influence on the overall efficiency of thermoacoustic systems, yet they are still not quantified sufficiently for practical thermoacoustic applications. Current paper addresses these issues through developing appropriate measurement methodologies which could be applied to “model” thermoacoustic devices in order to study the fundamental fluid flow behaviour. As a first step, and an illustration of the measurement capabilities, it focuses on the flow at the extremity of the stack of parallel plates. It is thought that the flow behaviour in this region plays an important role in heat transfer processes between the stack and the heat exchangers, and so the proposed measurement techniques and experimental results are of both fundamental and practical importance.

## 2 Literature review

Particle Image Velocimetry (PIV) has been successfully applied in great many areas of fluid mechanics; it is rather impractical to provide a detailed discussion here. Comprehensive reviews are available [4,5], while Measurement Science and Technology devoted a series of special issues and “features” to the subject [6-11] with over 70 research papers. Nowadays, PIV is considered a mature measurement technique, with many turn-key systems available on the market. The research challenge is therefore a continuous improvement of the accuracy and data interpretation methods as well as application of the PIV techniques to complex (often non-linear) systems. In the context of thermoacoustic engines and refrigerators the two technical challenges are to devise appropriate triggering/data sampling techniques that would enable defining reliably the measurement points within the acoustic cycle and data processing methods that would allow extracting average features of the resulting flow field and the statistical analysis which would characterise the unsteady characteristics of the flow.

The above mentioned challenges are in some way similar to those of PIV imaging in internal combustion engines [12-14], where the flow must be sampled at selected phase angles of the engine cycle, while unsteady flow behaviour must be analysed through ensemble averaging over many cycles, rather than by the analysis of temporal signals, as is usually the case in steady flows – see the discussion provided by Towers and Towers in [5], pages 354-355, and in [12]. However, while measurement phase-locking is relatively straightforward for IC engines (e.g. crank angle), in thermoacoustics one needs to rely on the timing of the acoustic excitation to trigger the PIV imaging, which can be achieved by several different methods. This adds additional complexity to the measurement as well as potentially some measurement uncertainty.

Applications of PIV for flow visualization or velocity measurement in acoustic systems were reported by Hann and Greated [15,16] who used a double exposure on a single frame and an auto-correlation method. Campbell et al. [17] carried out a review of PIV (as well as LDA) methods in sound measurement applications, and focused in particular on measurements illustrating streaming effects in acoustic systems using PIV. More recent work by Nabavi et al. [18] focused on simultaneous measurement of acoustic and streaming velocities at selected phases of the acoustic cycle, the former obtained by cross-correlating two consecutive PIV images, while the latter was obtained by cross-correlating the alternative PIV images at the same phase. A good agreement between experiments and theoretical predictions was reported. A somewhat similar approach was adopted by Debesse et al. [19] who measured acoustic and streaming velocities in a high pressure (7 – 15 bar) standing wave resonator working with nitrogen at a frequency of 22 Hz. Here the acoustic excitation was induced by a thermoacoustic engine located at one end of the resonator, while the velocity fields were measured at the other end, through a short cylindrical section made out of glass.

The flow field around internal structures of thermoacoustic systems was perhaps first investigated by Blanc-Benon et al. [20]. They used a quarter-wavelength thermoacoustic refrigerator configuration, driven by a loudspeaker at a frequency of 200 Hz. The experiments were conducted for two stacks: one with plate thickness of 0.15 mm and plate spacing of 1.0 mm, the other with plate thickness of 1.0 mm and plate spacing of 2.0 mm. The drive ratios were relatively low: 1.5% and 1.0%, respectively. The measurements were locked onto the loudspeaker signal. Vortex structures around the edges of stack plates were obtained by averaging of 100 PIV images taken at selected phases of the acoustic cycle (altogether 16 phases in an acoustic cycle were investigated). The results showed both concentrated and elongated eddies, which nevertheless remained attached to the plates. Further investigations of velocity fields generated by the oscillatory flow past the parallel-plate stacks were carried out by Castrejón-Pita et al. [21], Berson and Blanc-Benon [22], Berson et al. [23], Mao et al. [24], Aben et al. [25] and Jaworski et al [26]. Generally speaking all these works focused on velocity and vorticity fields in order to classify the flow morphology as a function of stack

geometries and acoustic excitation levels. Some similarity criteria have also been suggested to find the controlling parameters for this type of flow.

Unfortunately, so far only the mean velocity and vorticity fields obtained by ensemble-averaging were investigated. Current work is driven by the interest in the fluid-mechanical aspects of the thermoacoustic systems, in particular the turbulence characteristics in the vicinity of the parallel-plate thermoacoustic stack, which may have a strong impact on the actual heat transfer intensity. The mean flow field features investigated experimentally [20-26] have been successfully replicated by various numerical works (see for example [20, 27-30]). Unfortunately, there is a fundamental problem here since CFD typically uses time-dependent solutions of Navier-Stokes equations, which after a few cycles converge to numerically stable (i.e. highly repeatable) flow patterns. Unfortunately, the data presented in this paper shows that the real flow field is highly unsteady in the sense that the cycle-to-cycle variations are significant. The similarity between actual measurements and CFD only arises when ensemble-averaged data is compared to time-dependent but “numerically stable” results of CFD. In this sense CFD can reproduce well the mean flow field. Neither statistical velocity fluctuations nor small-scale eddies contained in the flow field and possibly generated by dissipating the large scale vortices were reported. Another difficulty is that the flow conditions investigated by CFD have relatively small Reynolds and/or Mach numbers, which rarely promotes the occurrence of turbulence. As a result very little is known about the nature of turbulence in oscillatory flows as investigated in the present work, which is hoped to provide an important first step for further experimental work and some more advanced numerical studies.

### 3 Experimental apparatus and measurement techniques

The detailed description of the rig and its linear acoustic model is given in [31], while the PIV measurement technique is briefly introduced in [24]. Therefore only essential information is provided to maintain the paper clarity. On the other hand, some new information is included in areas such as the analysis of seeding particles or triggering of the measurement system due to the specific nature of the journal.

#### 3.1 Resonator and stacks

Figure 2a shows a schematic diagram of the experimental rig with the main components and their dimensions. The working gas is air at atmospheric pressure and room temperature. The oscillatory flow is induced by a standing acoustic wave generated by a loudspeaker. The coupling of the square duct and the loudspeaker enables the rig to work as a quarter-wavelength resonator with the fundamental frequency of 13.1 Hz. Current experiments were carried out at drive ratios up to 3%. Construction of the rig described above allows testing arbitrary stack arrangements, at arbitrary locations along the resonator. In the current work, two stacks were tested, both of which had the length,  $l = 200$  mm and the width to fit the internal resonator width. The first stack (denoted as Stack I) had  $d = 1.1$  mm thick plates, with the spacing between plates  $D = 5.0$  mm. The second stack (denoted as Stack II) had  $d = 5.0$  mm thick plates, with the spacing between plates  $D = 10$  mm (see Figure 2b for a stack schematic). The fluid particle displacement amplitude is normally less than half of the plate length, therefore the flow disturbance from one end of the stack plates is considered too far to disturb the flow at the other end of the stack (in other words the plates can be assumed “semi-infinite” in length). For both stacks, the distance separating the centre of the stack and the end plate of the resonator was 4.11 m.

### 3.2 Flow seeding and laser illumination

Air in the resonator is seeded with olive oil droplets of sizes typically around  $1\ \mu\text{m}$ . The particle suspension was injected through an opening in the resonator wall, close to the location of the stack, while another opening far from the measurement zone allowed maintaining the atmospheric pressure inside the resonator. After the seeding was in place, the openings were blocked and a high intensity acoustic wave was used to distribute the particles evenly within the measurement zone, after which the actual imaging was undertaken. After the tracer injection a high tracer particle density of more than 15 particles in each interrogation spot in average can be obtained, which enables a relatively high detection probability of a valid velocity vector [32]. This quality particle suspension lasts typically for a period of a few minutes, during which the PIV measurements are undertaken. After a few minutes, the particles tended to settle, adhere to the internal surfaces or drifted away most likely due to streaming processes. Subsequently the rig had to be cleaned inside and the seeding had to be re-applied before the next set of experiments.

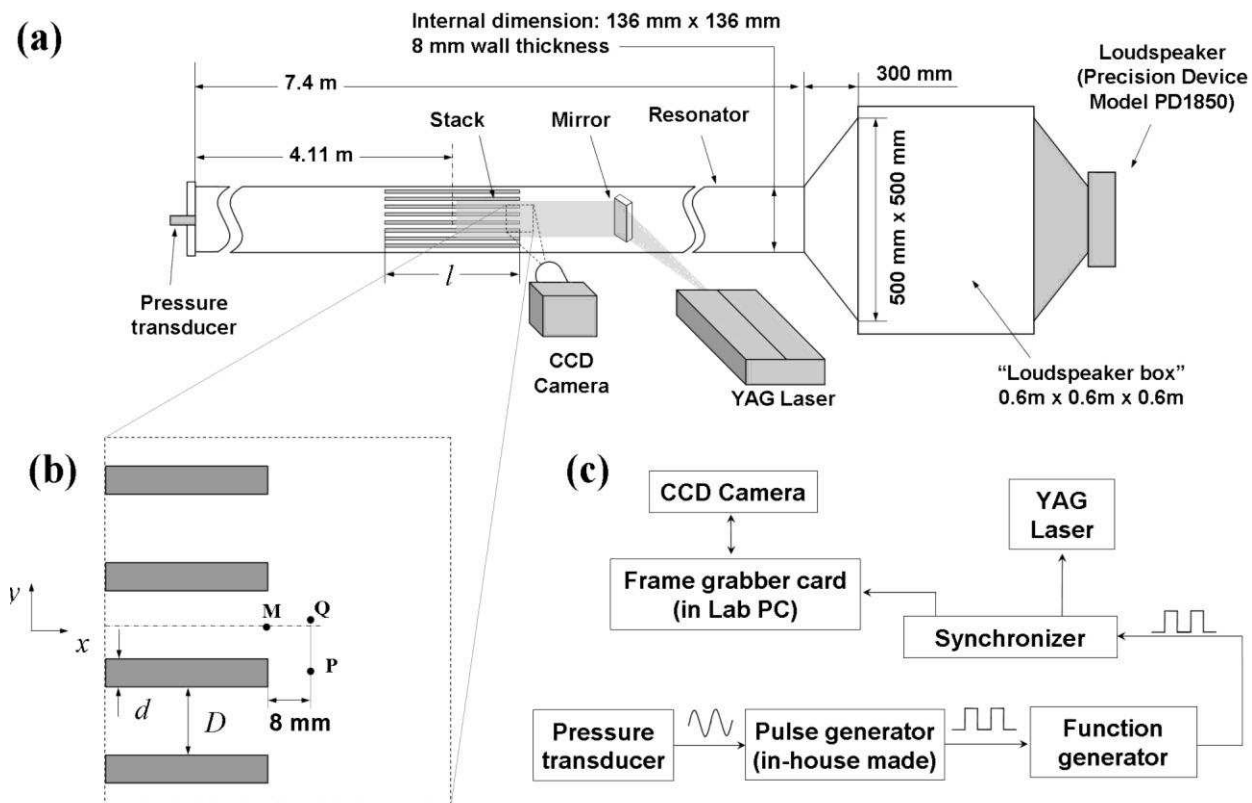


**Figure 2** Schematic of experimental apparatus (a); details of the stack and imaging area (b); and block diagram of the triggering mechanism used for phase-locking in PIV measurements (c)

In the PIV measurement of the velocity field, it is the velocity of the particles suspended in the fluid that is actually measured. Therefore, it is necessary for the particles to follow the flow faithfully. The unsteady motion of dispersed particles suspended in a continuous medium was modelled by Melling [33] (cf. Eq. (2) in [33]). According to King [34] there are also additional forces induced by the acoustic radiation pressure (cf. Eq. (76) in [34]) in a standing wave. However in the experimental conditions considered, the acoustic radiation pressure on the tracer particle is about seven orders of magnitude smaller than the acceleration force according to Stokes' law and it may be easily neglected here. Using the analysis by Melling [33], and considering that, in this case the particle density  $\rho_p$  and the fluid density  $\rho$  differ by three orders of magnitude, one can simplify Melling's equation to

$$\frac{\pi d_p^3}{6} \rho_p \frac{du_p}{dt} = -3\pi\mu d_p (u_p - u) \quad (1)$$

where  $d_p$  is the particle diameter,  $\mu$  (about  $1.81 \times 10^{-5} \text{ kg m}^{-1} \text{ s}^{-1}$  for air at 1atm and  $20^\circ \text{C}$ ) is the dynamic viscosity of the fluid,  $u_p$  and  $u$  are the instantaneous velocity of the particle and fluid respectively. Of course  $u$  is a nonlinear function of time in the unsteady flow around the stack plates and the equations of motion become difficult to solve. Relaxation time,  $\tau_s$  could be used to measure the tendency of the particles to follow the fluid velocity, on the assumption that the particle velocity approaches the flow velocity exponentially, as described by Eq. (2.3) in [35]. The relaxation time  $\tau_s$  is defined as

$$\tau_s = \frac{d_p^2 \rho_p}{18\mu} \quad (2)$$

Assuming that the particles follow the flow if  $u_p/u > 0.99$ , with no more than  $1^\circ$  phase lag, it can be shown that the maximum diameter of the particles should be about  $4.0 \mu\text{m}$  for the acoustically driven oscillatory flow of interest ( $f = 13.1\text{Hz}$ ). Therefore the choice of the smoke generator and the resulting particles used for PIV measurements seem reasonable.

A laser beam from a Nd:YAG pulsed laser (BigSky Laser) was expanded to form a divergent laser sheet in the vertical plane (Fig. 2a). It penetrated into the resonator perpendicularly to the resonator axis and was reflected by a small rectangular mirror ( $30 \text{ mm} \times 10 \text{ mm}$ ) to illuminate the flow into and out of the stack. The mirror was installed  $0.7 \text{ m}$  away from the end of the stack, while the laser aperture was about  $0.3 \text{ m}$  away from the mirror; the imaging area was approximately in the beam waist, where the laser sheet is about  $1 \text{ mm}$  thick, measured by using ‘‘paper burn’’ technique. It was confirmed by a preliminary PIV measurement (not shown here) that the presence of the mirror had no discernible effect on the oscillatory flow at the stack.

### 3.3 Details of PIV measurement

Figure 2c shows a block diagram of the PIV triggering mechanism used in the current study. The output signal of the pressure transducer shown in Figure 2a is used as a phase reference to generate a TTL pulse sequence by an in-house made circuitry, at the same frequency as the acoustic excitation provided to the loudspeaker. The TTL signal was used to synchronize the laser pulses and the image capturing by a 4MP camera, so that the pictures were phase-locked to the pressure oscillation, thus the velocity oscillation in the resonator. The phase of the TTL signal can be shifted so that the flow in different phases of the acoustic oscillation can be observed. As schematically shown in Figure 3, 20 phases (every  $18^\circ$ ) were investigated in each acoustic cycle. Here the times when these 20 phases ( $\Phi_1, \Phi_2 \dots \Phi_{20}$ ) appear is shown relative to the mean ensemble averaged velocity at point M (cf. Fig. 2b). In general, the flow corresponding to phases  $\Phi_1 - \Phi_{10}$ , when the fluid flows out of the stack with a positive velocity, is referred to as the ejection stage, while the flow corresponding to phases  $\Phi_{11} - \Phi_{20}$ , when the fluid flows into the stack with a negative velocity, is referred to as the suction stage – both explained in more detail in section 4.3.

To determine the flow velocity in each phase, pairs of singly exposed images were captured. The time difference of images in each pair was determined by the laser pulse separation, which was chosen so that the particle displacements during the interval were generally not more than  $1/4$  of the interrogation area used to analyze the captured images [36]. Thus, the time separations between laser pulses were varied according to the velocity magnitude

at the investigated phase, and the size of the investigated fields. A flow field of smaller size was imaged to reveal the velocity gradient in the viscous boundary layer, while a larger size was applied to view the general pattern of the wake flow. The measured field size ranged from 25 mm × 25 mm to 60 mm × 60 mm for the investigated two stack configurations.

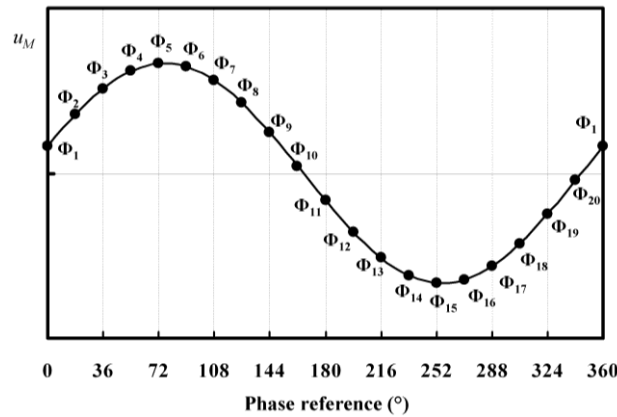


**Figure 3 Phase-averaged velocity oscillation at point M and corresponding phases at which the PIV measurements are taken**

The image processing was performed using commercial software (TSI INSIGHT™). A standard Fast Fourier Transform (FFT) cross-correlation algorithm was used and Gaussian peak detection algorithm was applied to identify the velocity vectors. The interrogation spots had a size of 32 × 32 pixels, and were recursively reduced to 16 × 16 pixels with 50% overlap [37]. A validation was applied on the obtained velocity vector fields to remove spurious vectors. The spurious vectors are detected by using a “neighbourhood mean” filter, which removes vectors that are out of the range of the mean value +/- three times standard deviation in a window of 3 × 3 vectors. A median value is used rather than the mean to exclude any contribution from a spurious vector that may be present in the third row or column in the 3 × 3 window, in the row-by-row scanning process.

## 4 Results and discussion

### 4.1 Validation of velocity measurement

PIV is an absolute method of velocity measurement, which relies on the displacement of tracer particles as captured by two consecutive images with known time separation. Nevertheless it seemed useful to validate the velocity measurement in two ways. Firstly, an acoustic wave was established in an empty resonator. Given that the pressure amplitude at the end of the resonator is known, it is easy to predict analytically the oscillatory velocity field in the centre of the resonator (at any axial location, for example in the location where the stack would normally reside). These measurements simply confirmed that the measurement and data acquisition setup was working correctly. The absolute values of discrepancy between the predicted and measured velocity values at different phases were typically less than 3.6% of the velocity amplitude.

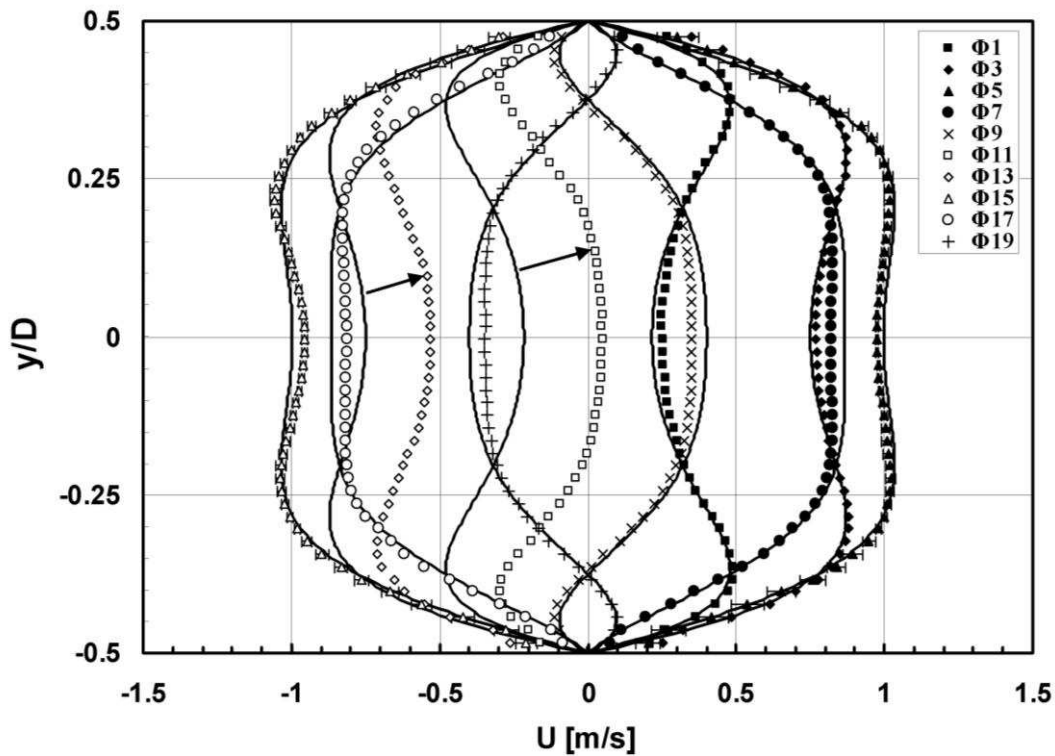


**Figure 4 Velocity profiles for 10 phases in the cycle: solid lines – theoretical predictions; symbols – ensemble averaged measurements. Data shown for Stack II at  $2.4D$  from the channel entry and  $Dr$  of 0.3%; arrows indicate the discrepancy between measured and theoretical profiles for  $\Phi_{11}$  and  $\Phi_{13}$ ; error bars for  $\Phi_{5}$  and  $\Phi_{15}$  show the standard deviation based on averaging of 100 PIV measurements**

Secondly, ensemble averaged velocity measurements were carried out within a selected channel between two stack plates and compared to theoretical predictions. It is known that the flow velocity in the stack channel at a relatively low drive ratio can be predicted accurately by the linear thermoacoustics theory [1]. Figure 4 shows the velocity distribution of the  $U$  component of the velocity for 10 selected phases, obtained by PIV measurements of the flow around the end of Stack II, along with the profiles predicted by linear thermoacoustics. The measured velocity profiles were obtained at the distance of  $2.4D$  into the channel. The  $y$  coordinate is normalized by the channel width  $D$  shown in Fig. 2. The selected case was measured at  $Dr = 0.3\%$ , which corresponds to the velocity amplitude of about 1.05 m/s. It can be seen that the measured mean velocity profiles reproduce very well the double boundary layers typically found in the oscillatory flows and the velocity magnitudes, except for  $\Phi_{11}$  and  $\Phi_{13}$  (see arrows in Fig. 4). The differences between measured and predicted velocities in these phases are caused by the entrance effects, which occur during the suction phase of the oscillatory flow [26]. Velocity profiles for  $\Phi_{5}$  and  $\Phi_{15}$  have also “error bars” corresponding to the standard deviation of velocity values obtained on the basis of averaging 100 measurements. Generally, the standard deviation is less than 2% of the mean velocity amplitude in the central region of the channel. A higher fluctuation level in the boundary layer is probably caused by the wall-drag effect on the seeding particles in the vicinity of the solid boundary, which is well known to be highly nonlinear [38, 39]. Since the distance to the wall of any seeding particle position is a random variable, the strong nonlinearity leads to high fluctuations in velocity as inferred by the FFT/cross-correlation algorithm.

The velocity profiles of the oscillatory flow in a channel between two parallel plates are conceptually similar to those for the oscillatory flow in a circular pore, which is also often referred to as the Womersley profiles due to his pioneering work [40]. Nevertheless the analytical expressions for the velocity profiles in the oscillatory flow in pores of

a range of different geometries, such as square, circular and triangular shapes, as well as a channel between two parallel planes are available from Arnott [41].

## 4.2 Ensemble averaging of velocity field

For a typical experimental run, an arbitrary number,  $N$ , of instantaneous flow fields can be obtained for each of the 20 phases. Therefore the data set obtained for each case consists of  $20 \times N$  instantaneous flow fields. Each instantaneous flow field provides two velocity components  $u(x, y, \Phi, i)$  and  $v(x, y, \Phi, i)$  in a spatial point  $(x, y)$ , at phase  $\Phi$  of each acoustic oscillation cycle  $i$ .

The classical Reynolds decomposition is used to separate the instantaneous flow fields into mean (ensemble-averaged) flow fields and their fluctuations, based on the assumption that the mean velocity fields are the same at any time corresponding to the same phase in the acoustic cycle [42]. Therefore, from a group of instantaneous flow fields of the same phase, the corresponding mean velocities  $U(x, y, \Phi)$  and  $V(x, y, \Phi)$ , and the RMS values (standard deviation) of the velocity fluctuations,  $u'(x, y, \Phi)$  and  $v'(x, y, \Phi)$ , for each phase  $\Phi$  can be calculated as follows:

$$U(x, y, \Phi) = \frac{1}{N} \sum_{i=1}^N u(x, y, \Phi, i) \quad (3)$$

$$V(x, y, \Phi) = \frac{1}{N} \sum_{i=1}^N v(x, y, \Phi, i) \quad (4)$$

$$u'(x, y, \Phi) = \sqrt{\frac{1}{N} \sum_{i=1}^N (u(x, y, \Phi, i) - U(x, y, \Phi))^2} \quad (5)$$

$$v'(x, y, \Phi) = \sqrt{\frac{1}{N} \sum_{i=1}^N (v(x, y, \Phi, i) - V(x, y, \Phi))^2} \quad (6)$$

where the summation is over  $i = 1, \dots, N$  images taken at phase  $\Phi$ , and the prime indicates the fluctuation of a variable. Of course the RMS values of velocity fluctuations will contain both the uncertainty introduced by the measurement and the effects of the flow behaviour. Judging from the results shown in section 4.1 (and the results shown in later sections 4.3 and 4.4), the measurement uncertainty is relatively low compared to the component corresponding to true flow unsteadiness (1-2% vs. tens of % – cf. Figs. 9-12). Therefore, by using the traditional Reynolds decomposition one could separate the mean and fluctuating components of the instantaneous flow velocity, the latter containing all the unsteady features of the velocity field behaviour.

Of course it should be noted that turbulence is a three-dimensional phenomenon. However due to the limitations of the measurement (2D system) as well as the practicalities of the physical setup and access, the current study only focused on the plane parallel to the resonator axis. Nevertheless, for reference purposes, some measurements were performed to estimate the fluctuations of the third “out-of-plane” velocity component (typically denoted by  $w$ ). Here, the laser sheet was aligned perpendicular to the resonator axis (5 mm from the end of Stack II where the fluctuations were found to be the highest), while the camera recorded the image reflected in the mirror shown in Figure 2. The maximum measured values of  $w/U_a$  were about 12%, compared to 40% in  $(u^2+v^2)^{0.5}/U_a$ , 29% in  $u'/U_a$  and 28% in

$v/U_a$ ,  $U_a$  being the amplitude of the mean velocity in x direction. This occurred when the fluid is moving out of the channel with the velocity magnitude near to its amplitude. Although the “out-of-plane” fluctuations are clearly much lower than those in  $u$  and  $v$ , the results emphasise that in order to model the flow behaviour correctly any future CFD modelling aiming to capture the turbulence physics correctly may have to be fully three-dimensional – this point being an addition to the discussion at the end of Section 2.

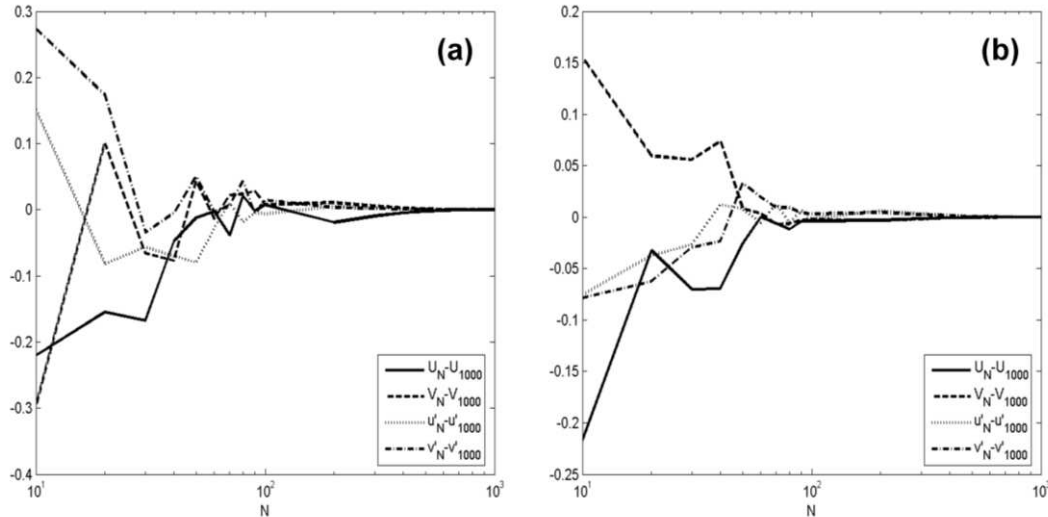


**Figure 5 Effect of the number of instantaneous measurements,  $N$ , on the computation of the flow statistics at point P (a) and point Q (b). Note: units of vertical axes are in m/s for all variables. Index  $N$  indicates the number of PIV images taken to calculate a given statistic: either mean velocity or velocity fluctuation.**

An important step in developing the measurement methodologies for characterising oscillatory flows is to establish the number of instantaneous images for a reliable determination of mean flow features. Some studies [43] indicate that to reliably measure turbulence characteristics 1000 frames had to be used, while others rely on substantially smaller number of frames: Cenedese et al. [44] used only 40 frames for extracting the steady mean flow features. In somewhat conceptually similar studies of average helicity and energy dissipation in a turbulent swirling jet, Regunath et al. [45] argued that 500 frames was sufficient for their analysis. The effect of the number of instantaneous measurements pictures,  $N$ , on the flow statistics in the present measurement has been assessed by computing the statistics using up to 1000 frames. The 1000 frames were taken for Stack II, at phase  $\Phi_4$ . The result is shown in Fig. 5, corresponding respectively to point P which is along the centreline of the plate, and point Q in Fig. 2b (Q is located 9 mm above P). It is observed that a very good convergence is obtained for 1000 frames. For only 100 frames, the convergence is not rigorously reached, yet is judged sufficient to obtain a good representation of the flow over the whole flow field, and a reasonable representative of the convergent statistics. This was the reason for using  $N = 100$  frames in the current study, and this choice seemed also a reasonable trade off between the accuracy and the storage capacity and data processing power available.

### 4.3 Comparison between the instantaneous and averaged flow features

The detailed flow physics of the oscillatory flow in the experimental setup discussed in this paper has already been given in reference [24], based on the averaged flow field analysis. It will not be repeated here. It is perhaps important to note that there are two main stages in the oscillatory flow around a stack of plates: The first is the

“ejection” stage, where the flow is in the positive direction (cf. Fig. 2) and the fluid emerges from the channels (phases  $\Phi 1$ -  $\Phi 10$ ). Here typically the flow separates at the edges of the plates, and various types of vortical structures are rolled up. These may be shed into the flow if the drive ratio is large enough, or may remain in the plate vicinity for small drive ratios. Figures 6d and 7d, discussed later give a general idea about the type of vortex shedding occurring in the experiments. The patterns may resemble the classical von Karman vortex street, although there are clear differences in that the flow is not steady and is accelerated and decelerated in the half cycle discussed here. The exact features of the vortex shedding depend on the flow forcing and the geometry of the stack; although various similarity numbers have been suggested in [24]. The second stage of the flow is the “suction” stage, where the flow is in the negative direction (phases  $\Phi 11$ -  $\Phi 20$ , also cf. Fig. 2). During this period all the vortex structures generated in the “ejection” stage (or their remains if they had time to dissipate) impinge back on the stack plates. Figure 8d discussed later illustrates the impingement of vortex structures onto the stack.

It is thought that these alternate processes of vortex shedding, flow reversal and vortex “re-impingement” are critical to the understanding of the heat transfer modes between the stack and the heat exchangers (not studied in the current work). Previous work devoted to analysing flow patterns in the oscillatory flow past a stack of plates [20-26] has focussed on the mean flow features and tacitly assumed that by taking a sufficient amount of instantaneous images for ensemble averaging any variability of the flow between cycles would be smoothed out. However this approach may be questionable especially if the instantaneous flow features are very different from the averaged ones, which may in turn have implications on the heat transfer predictions. So far no attempt has been made to quantify that cycle-to-cycle flow variability or to estimate to what extent are the instantaneous flow features different from the averaged ones. For ease of the following discussion, the flow field data will be presented in terms of vorticity maps, rather than velocity field.

Figure 6 shows an example of comparisons between the instantaneous vorticity field (three images have been selected at random from a string of 100 and shown as Figs. 6a – 6c) and the averaged vorticity field (Fig. 6d) for Stack II. Here the drive ratio is relatively low: 0.6 %, the selected phase is  $\Phi 6$ . In the references mentioned above, this type of flow pattern is referred to as symmetrical attached vortices on the basis of the averaged vorticity field. However it is clear from the instantaneous images that the main vortices shed from the plate behave in a somewhat unsteady manner: they assume different shapes, strengths and spatial locations. In the ensemble-averaged vorticity field these features are simply filtered out, as are some of the small-scale vortex structures, present in the flow field.

Figure 7 shows similar comparison between the instantaneous and averaged vorticity fields for Stack II at a significantly higher drive ratio of 2.0%, for a selected phase angle  $\Phi 8$  (note that this is a “zoomed-out” view compared to Fig. 6). It can be seen that while the instantaneous images show a degree of chaotic behaviour and a multitude of vortex scales, the ensemble-averaged image in Fig. 7d still brings out an orderly von Karman-like vortex pattern, albeit with somewhat smaller vorticity magnitudes and spatially “smoothed out”. Figure 8 shows similar comparisons between instantaneous and ensemble averaged flow fields for Stack I and  $Dr = 1.0\%$ , except that phase  $\Phi 12$  has been chosen, in order to illustrate the impingement of vortex structures back onto the stack, taking place in the suction phase of the cycle.

The vorticity maps shown in this section clearly show that vortex shedding processes are stochastic in the sense that vortex strength, size and location are random and could be classed as quasi-periodic in nature (unlike the well known von Karman vortex shedding). The latter is particularly clear when analysing the Fourier transforms of point-wise hot-wire measurements in the wake of the plate as already shown in reference [24]. Unfortunately, this feature could not be brought out in the current PIV study because the system repetition rate is too low to look at a single cycle at high temporal resolution.

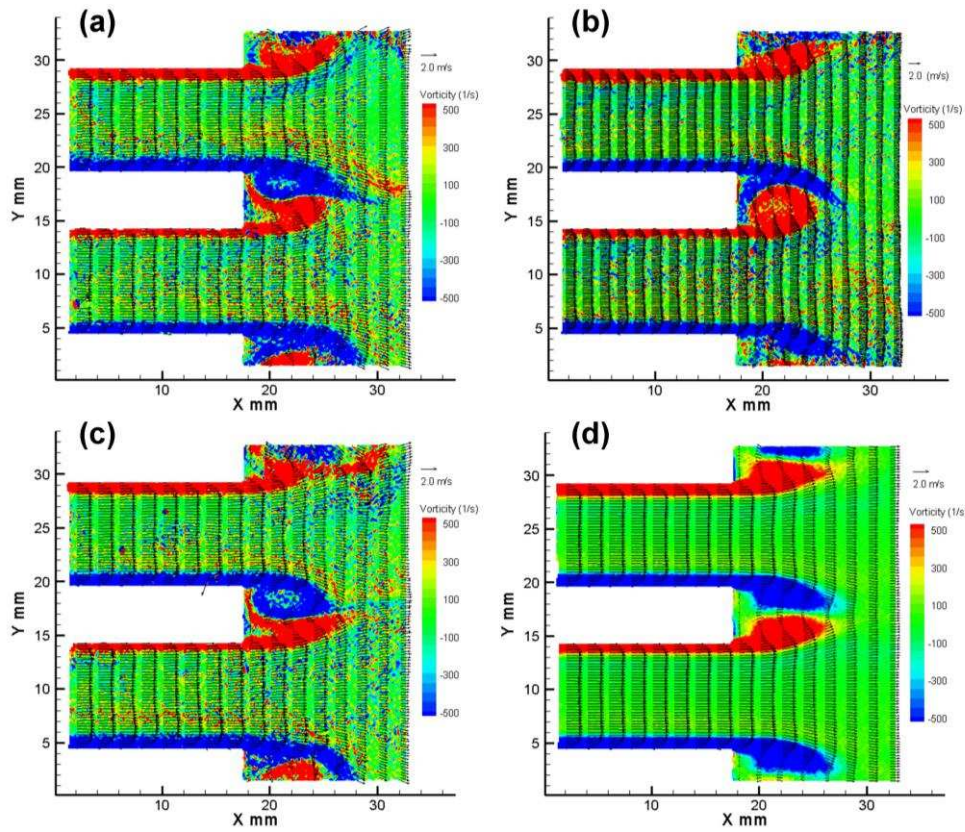


Figure 6 Illustration of the variability between vortex structures in three instantaneous images of the vorticity field (a, b and c). The average vorticity field resulting from ensemble averaging of 100 instantaneous images (d).

Stack II,  $Dr = 0.6\%$ , phase  $\Phi 6$ .

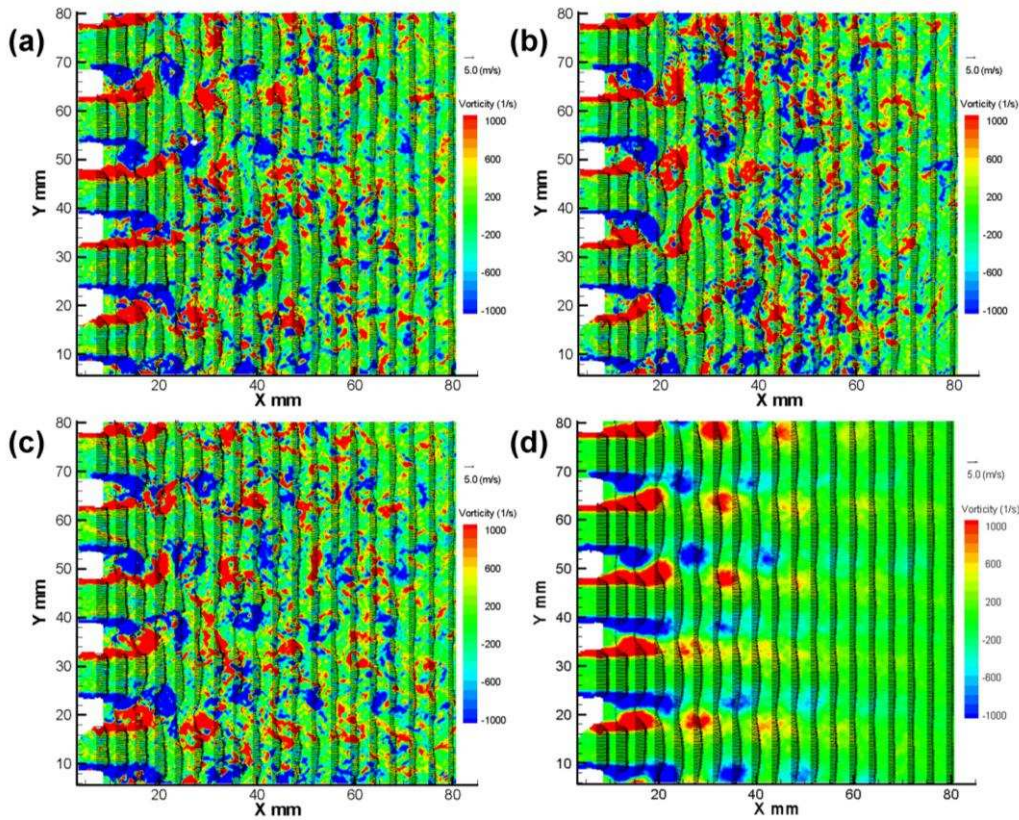
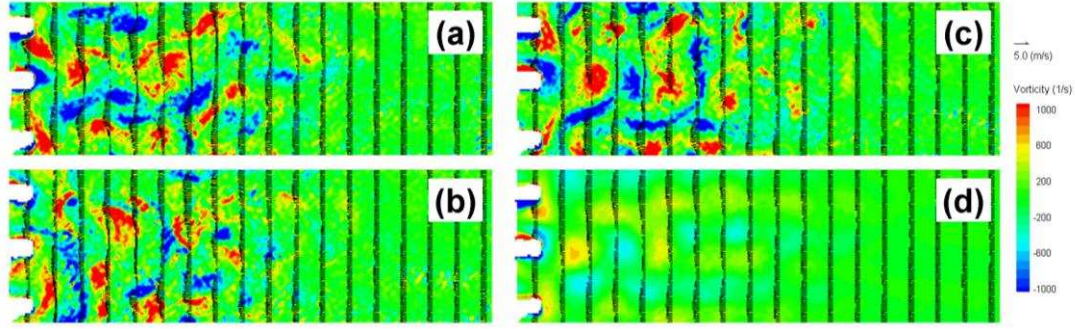


Figure 7 Illustration of the variability between vortex structures in three instantaneous images of the vorticity field (a, b and c). The average vorticity field resulting from ensemble averaging of 100 instantaneous images (d).

Stack II,  $Dr = 2.0\%$ , phase  $\Phi 8$ .



**Figure 8 Illustration of the variability between vortex structures in three instantaneous images of the vorticity field (a, b and c). The average vorticity field resulting from ensemble averaging of 100 instantaneous images (d). Stack I,  $Dr = 1.0\%$ , phase  $\Phi_{12}$ .**

#### 4.4 Turbulence vs. “total fluctuation” intensity - spatial distribution

As already mentioned in Section 4.2, for the cyclic flows as discussed in our paper, calculation of the time-series statistics (even if high speed PIV was available) makes little sense due to the time dependence of the underlying mean flow. Therefore it is usually assumed that the processes are ergodic and the data is collected at a fixed instant (phase) for a set of different cycles in order to calculate the flow statistics at that selected phase. In the classical description of turbulent flows, the RMS values of velocity fluctuations as defined by equations (5) and (6) lead to the concept of “turbulence intensity” using an appropriately selected reference velocity from the mean flow. However, as discussed below, such calculations tend to take into account the unsteadiness introduced by the large scale coherent structures together with the contributions from small scale vortex structures usually understood as “turbulence”. This distinction may be important from the point of view of heat transfer modelling that may be the ultimate objective in the thermoacoustic context.

Therefore for the purpose of this paper it is proposed to use somewhat different terminology: the velocity fluctuations described by equations (5) and (6) would give rise to a “fluctuation intensity”. This is denoted as  $T$  (with appropriate indices as necessary) and calculated using the classical concepts of “turbulence intensity”. On the other hand, appropriately spatially filtered velocity fields (as described later in section 4.5) would give rise to “small-scale turbulence intensity” (denoted as  $\theta$ ), understood as the contribution from vortex structures smaller than a certain cut-off length-scale.

In view of the instantaneous and averaged PIV images discussed in the previous section, this section attempts to present a statistical description of the unsteady processes of vortex shedding occurring in the oscillatory flows, using the concept of the abovementioned “fluctuation intensity”. Using the approach proposed by Pai [46] (for the classical turbulence intensity) the “fluctuation intensity” could be similarly defined as:

$$T_x = \sqrt{u'^2} / U^* ; T_y = \sqrt{v'^2} / U^* ; T_z = \sqrt{w'^2} / U^* ; \quad (7)$$

where the over-bar indicates a temporal mean function and  $U^*$  is a suitably chosen reference velocity. However, an alternative definition (also given by Pai [46]) suggests that the “fluctuation intensity” could also be defined as a sum of components in all directions according to the following formula:

$$T = \sqrt{\frac{1}{3}(\overline{u'^2} + \overline{v'^2} + \overline{w'^2})} / U^* . \quad (8)$$

Discussion in this section is limited to only a two-dimensional velocity field ( $u$  and  $v$ ) acquired from the 2-D PIV measurements. To enable the comparison of the level of velocity fluctuations for different velocity amplitudes and various stacks, the “fluctuation intensities” in  $x$  and  $y$  directions:  $T_x$  and  $T_y$  can be used (Eq. 7), where the reference velocity is simply the amplitude of the mean velocity in  $x$  direction,  $U_a$  (i.e. the acoustic velocity amplitude). However, it is perhaps somewhat easier to look at the combined quantity (total fluctuation intensity), by analogy to Eq. 8, which takes into account the velocity fluctuations in both  $x$  and  $y$  directions, namely:

$$T = \sqrt{u'^2(x, y, \Phi) + v'^2(x, y, \Phi)} / U_a . \quad (9)$$

Figure 9, shows the results of calculating the spatial distribution of  $x$  and  $y$  components of the fluctuation intensity within the PIV field of view for a selected case of Stack II, drive ratio  $Dr = 2.0\%$  and phase  $\Phi_8$  (i.e. the case presented in Fig. 7). In the example presented, it can be clearly seen that the level of velocity fluctuations in the  $y$  direction (Fig. 9b) reaches around 50% level, which is relatively high and comparable to total fluctuation intensities that may occur in strong vortex wakes and highly reversed flows. However, as indicated at the beginning of this section, the interpretation of plots such as in Fig.9b (or 9a) is not straightforward. It needs to be remembered that this particular type of flow contains a mixture of large-scale coherent structures (discrete eddies) and smaller scale structures (which one would normally refer to as “turbulence”). It seems reasonable to assume that the large variation of velocity from one instantaneous image to the next may well be caused by the variation in the position of the large vortices, not the intensity of small-scale velocity fluctuations. Furthermore, it can be hypothesised that a high level of the fluctuation intensity in Fig. 9b corresponds to relatively high lateral displacements of vortex structures from cycle to cycle, while somewhat smaller turbulence intensities appearing in Fig. 9a may indicate relatively lower level of longitudinal (stream-wise) variation in the position of discrete eddies from one cycle to another. However, the spatial distribution of  $x$  and  $y$  fluctuation intensities is relatively similar – therefore to simplify the results’ presentation in what is to follow, the total fluctuation intensity levels (Eq. 9) will be presented. For example graphs 9a and 9b become “combined” within the total fluctuation level  $T$  shown in graph 11d.

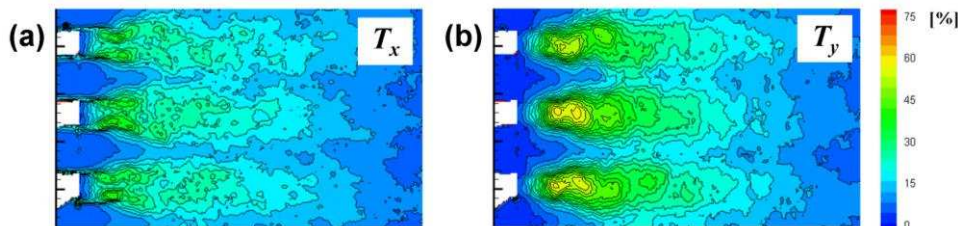


**Figure 9 Distribution of  $x$  and  $y$  components of fluctuation intensity:  $T_x$  and  $T_y$ ,; Stack II,  $Dr = 2.0\%$ , phase  $\Phi_8$ .**

Figure 10 shows the total fluctuation intensity distribution for six representative phases in the acoustic cycle for the case of Stack II and drive ratio  $Dr = 0.6\%$  (cf. Fig. 6), while Fig. 11 shows the total fluctuation intensity for six representative phases for the case of Stack II and drive ratio  $Dr = 2.0\%$  (cf. Fig. 7). Finally, Fig. 12 shows the total fluctuation intensity for six representative phases for the case of Stack I and drive ratio  $Dr = 1.0\%$ .

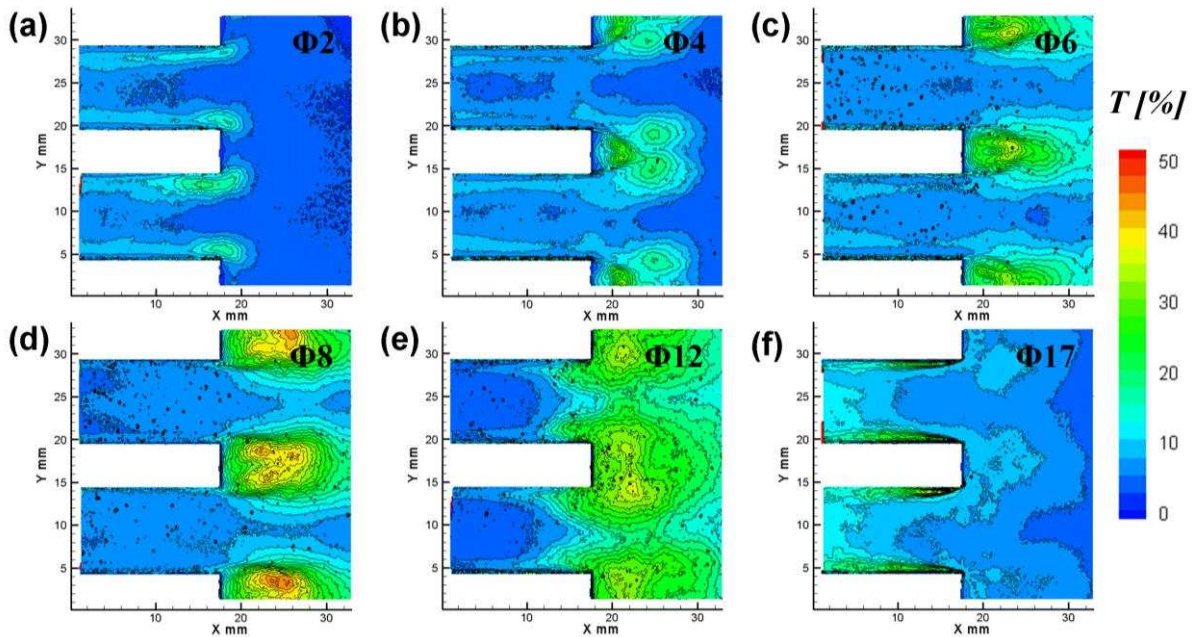


Figure 10 Distribution of the total fluctuation intensity,  $T$ ; Stack II,  $Dr = 0.6\%$ .

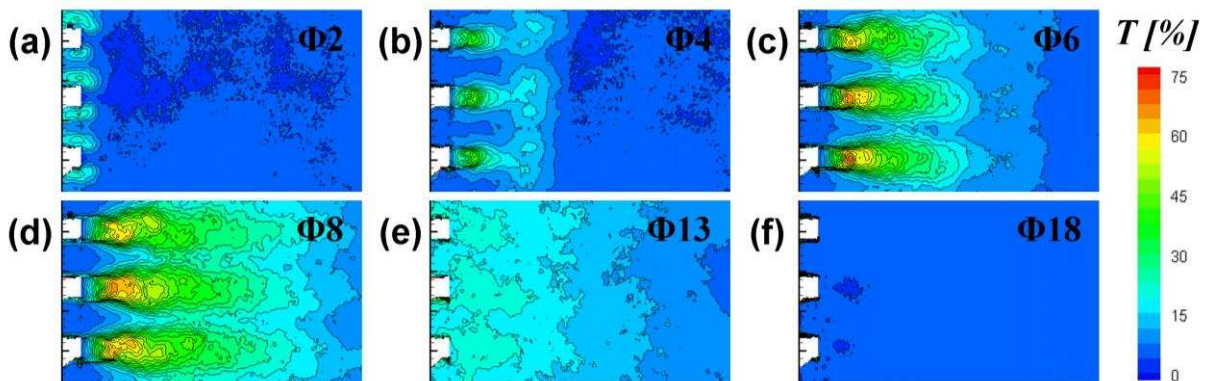


Figure 11 Distribution of the total fluctuation intensity,  $T$ ; Stack II,  $Dr = 2.0\%$ .

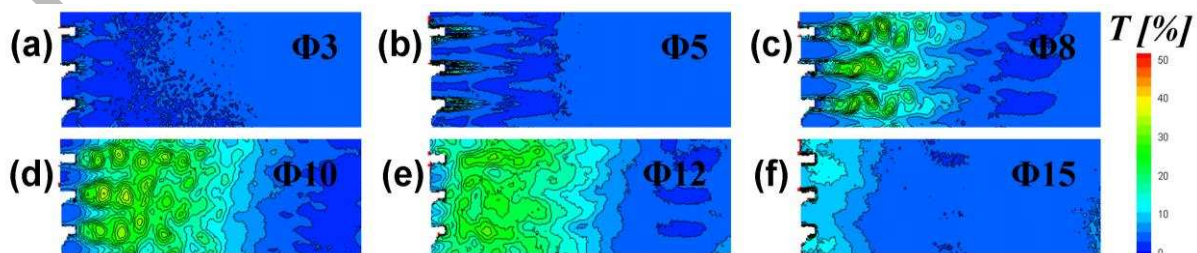


Figure 12 Distribution of the total fluctuation intensity,  $T$ ; Stack I,  $Dr = 1.0\%$ .

It is clear that the statistics of the velocity fluctuations in the oscillatory flow around the end of the parallel-plate stack is closely related to the main flow features discussed in section 4.3 and in particular mirrors the behaviour (and unsteadiness) of the coherent structures that are present in the mean flow. The high velocity fluctuations occur during the ejection stage and are located outside of the stack; the peak values generated usually between phases  $\Phi_6$  and  $\Phi_{10}$ , i.e. in the deceleration phases of the ejection cycle. It can also be easily seen by inspecting figures similar to Figs. 10 – 12 obtained for all experimental cases that the level of fluctuations grows with the drive ratio however there must be differences between absolute values of  $T$  and its spatial distribution for the two stacks tested here.

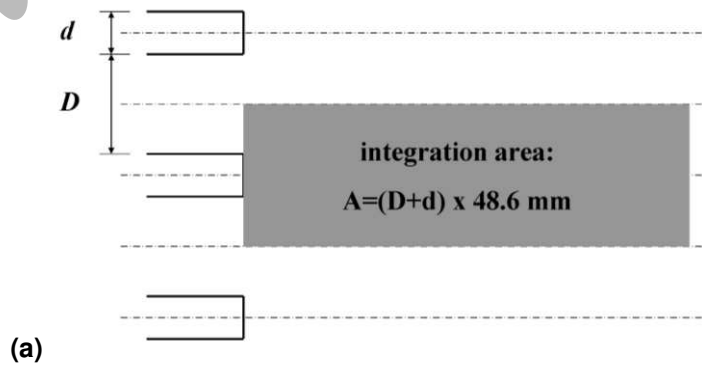
To have some overall measure of flow unsteadiness, the turbulence kinetic energy, defined as

$$k = \frac{1}{2}(\overline{u^2} + \overline{v^2} + \overline{w^2}) \quad (10)$$

can be analysed ( $w$  component is simply taken as zero in two-dimensional analysis). Strictly speaking this may have to be re-defined as “fluctuation kinetic energy” to follow the logic of “fluctuation intensities” described earlier. However it is not thought to be necessary for the purpose of this paper. An integral of  $k$  was calculated over an area corresponding to one plate segment, and extending from the plate’s end 48.6 mm out of the stack (this was the maximum field of view that was obtained in the experiments for Stack I), and then normalised by the area. Such approach is often used in meteorological studies such as [47] and [48]. Figure 13a illustrates schematically the integration area. For Stack I it is 6.1 mm wide, for Stack II it is 15 mm wide. The spatially averaged turbulence kinetic energy can be written as follows:

$$k_A = \frac{1}{A} \iint_A k(x, y, \Phi) dA. \quad (11)$$

Figure 13b shows the plots of  $k_A$  for all experimental cases as a function of phase in the cycle. As expected the energy is low for cases when the oscillation is weak (drive ratios 0.3% and 0.6% for both stacks), but becomes appreciable for higher drive ratios. It is also clear that its magnitude is higher for Stack II than for Stack I. This is again not surprising due to the fact that the separations on relatively thicker plates generally produce stronger concentrated vortices that contribute more strongly to fluctuation intensities. Finally it is possible to integrate the curves such as those shown in Fig. 13b over the oscillation cycle to obtain an area and cycle averaged turbulent kinetic energy (denoted  $k_{A,T}$ ), which is illustrated in Fig. 14. It is possible to interpret this graph as an indication of the total energy contained in the flow related to velocity fluctuations due to coherent structures and small scale turbulence.



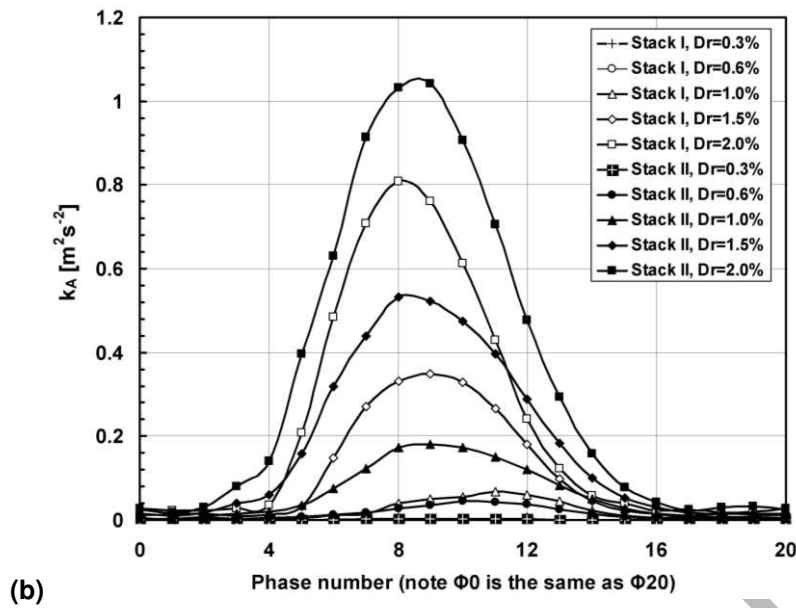


Figure 13 Illustration of the integration area for calculating averaged turbulent kinetic energy  $k_A$  over a sample area A (a); plot of  $k_A$  as a function of phase in the cycle for all experimental configurations (b).

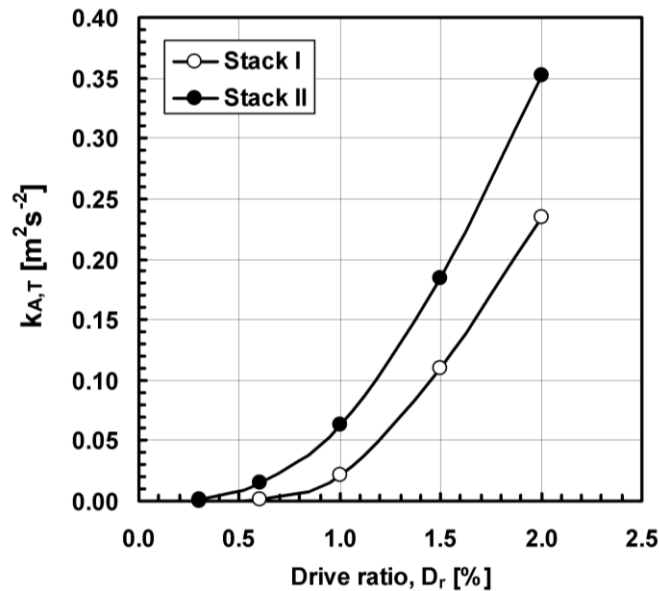


Figure 14 Area and cycle averaged turbulent kinetic energy  $k_{A,T}$  as a function of drive ratio.

#### 4.5 Separation of fluctuation intensity with regard to length-scales: small-scale turbulence intensity.

In the existing literature there have been many studies undertaken to investigate the effects of the turbulence intensity on heat transfer from solid bodies, such as circular cylinder [49,50], elliptical cylinder [50], and sphere [51] etc. For example, Kondjoyan and Daudin [50] studied the effect of the free stream turbulence intensity on the heat transfer coefficient on a circular cylinder and an elliptical cylinder when Reynolds number was between 5,000 and 30,000. The heat transfer coefficient,  $Nu$ , when the turbulence intensity is 40%, has a value of about two times its value when the turbulence intensity is 1.5%, which suggests that it is the small-scale turbulence (as opposed to large coherent structures) that is a major contributor to the heat transfer mechanisms. References [52,53] also investigated the effects that the integral length scale, which characterises the dimension of eddies in the flow, may have on the heat transfer.

Sak et al. [53] observed a decrease in the heat transfer coefficient, Nu, with the increase of the relative turbulence length scale from 0.5 to 1.47, when the relative turbulence intensity of the flow towards a circular cylinder is kept constant at about 6.7%. Since the turbulence scale may be an important contributor to the intensity of the heat transfer and the current study is intended as a precursor to turbulence characterisation in oscillatory flows, it seems appropriate to develop tools that could distinguish between the turbulence intensities contributed by various turbulence length scales present within the flow.

The instantaneous velocity  $u$  and  $v$ , following Reynolds decomposition and the definition in Eq. (3) – (6), are divided into the ensemble-averaged velocity and the fluctuation from the ensemble-averaged velocity:

$$u(x, y, \Phi, i) = U(x, y, \Phi) + u'(x, y, \Phi, i); \quad v(x, y, \Phi, i) = V(x, y, \Phi) + v'(x, y, \Phi, i) \quad (12)$$

The idea behind the data processing described below is that it should be possible to further divide the fluctuation component into large- and small-scale fluctuations according to a specified cut-off length  $\lambda$  related to the size of the eddies present in the flow:

$$\begin{aligned} u(x, y, \Phi, i) &= U(x, y, \Phi) + u'_l(x, y, \Phi, i, \lambda) + u'_s(x, y, \Phi, i, \lambda) \\ v(x, y, \Phi, i) &= V(x, y, \Phi) + v'_l(x, y, \Phi, i, \lambda) + v'_s(x, y, \Phi, i, \lambda) \end{aligned} \quad (13)$$

where  $u'_l$ ,  $v'_l$ ,  $u'_s$  and  $v'_s$  indicate the large-scale fluctuations and small-scale fluctuations of velocity components  $u$  and  $v$ , respectively.

The RMS value of the large-scale fluctuation ( $u'_l$  and  $v'_l$ ) and small-scale fluctuation ( $u'_s$  and  $v'_s$ ) would quantify the amount of the variation of each component at each phase at position  $(x, y)$  with cut-off length  $\lambda$ :

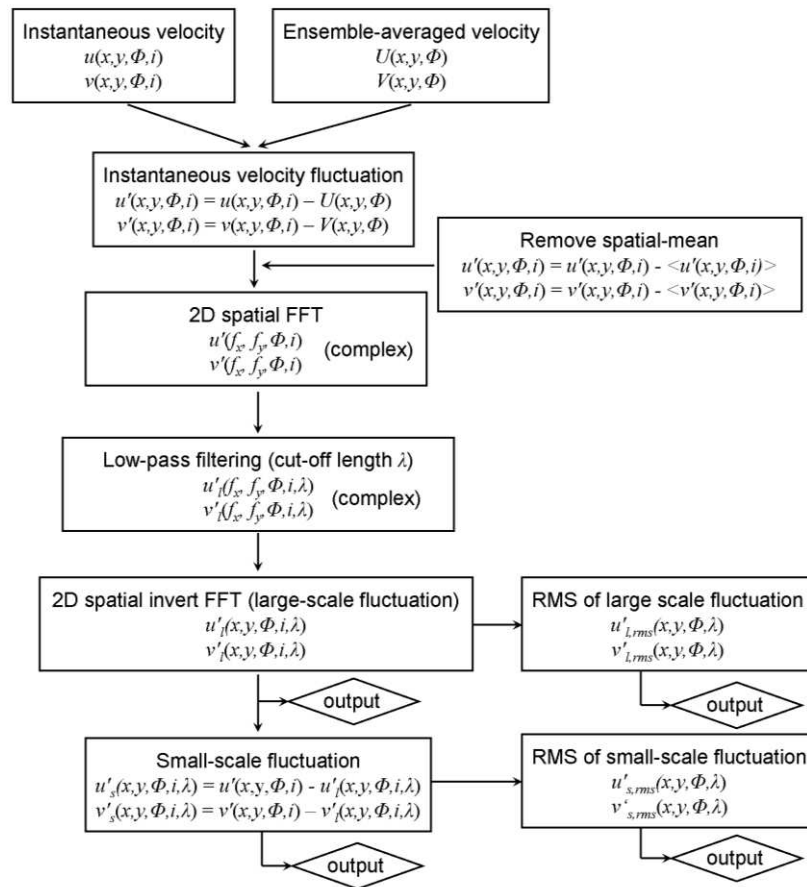
$$\begin{aligned} u'_{l,rms}(x, y, \Phi, \lambda) &= \sqrt{\frac{1}{N} \sum_{i=1}^N u'^2_l(x, y, \Phi, i, \lambda)}; \quad v'_{l,rms}(x, y, \Phi, \lambda) = \sqrt{\frac{1}{N} \sum_{i=1}^N v'^2_l(x, y, \Phi, i, \lambda)} \\ u'_{s,rms}(x, y, \Phi, \lambda) &= \sqrt{\frac{1}{N} \sum_{i=1}^N u'^2_s(x, y, \Phi, i, \lambda)}; \quad v'_{s,rms}(x, y, \Phi, \lambda) = \sqrt{\frac{1}{N} \sum_{i=1}^N v'^2_s(x, y, \Phi, i, \lambda)} \end{aligned} \quad (14)$$

Thus, a combined quantity to denote the amount of variation of velocity fluctuation at large-scale and small-scale can be respectively described by  $\sqrt{u'^2_{l,rms} + v'^2_{l,rms}}/U_a$  and  $\sqrt{u'^2_{s,rms} + v'^2_{s,rms}}/U_a$  (the latter according to the nomenclature introduced in section 4.4 could be denoted as  $\theta$ ). Their values are normalized by the amplitude of the mean velocity to indicate the relative strength.

In order to separate the small-scale and large-scale fluctuations of the flow, a two-dimensional spatial Fast Fourier Transform (FFT) technique has been designed, and the essence of the calculation algorithm is illustrated in Figure 15. The ensemble-averaged velocity field was first subtracted from the instantaneous two-dimensional velocity field to obtain the fluctuating velocity fields containing components  $u'(x, y, \Phi, i)$  and  $v'(x, y, \Phi, i)$ . Such “instantaneous fluctuating velocity fields” were then separated into  $u$  and  $v$  components and each was separately transformed using the FFT into the spatial-frequency domain. Figure 16 shows the 2D amplitude spectra computed from the instantaneous fluctuation ( $u'$ ,  $v'$ ) using 2D spatial FFT for the velocity field which is depicted in Figure 7c. Interestingly, the high intensity “peaks” in the centre form relatively regular patterns and it is thought that they correspond to large scale (low “wave-number”) coherent structures. Similar behaviour of the FFT was also observed by Piirto et al. [54] for vortex

shedding in steady flows. The rather random distribution of much lower amplitudes around the centre is thought to originate from the smaller scale (higher “wave-number”) eddies responsible for what was defined in section 4.4 as “small-scale turbulence”.

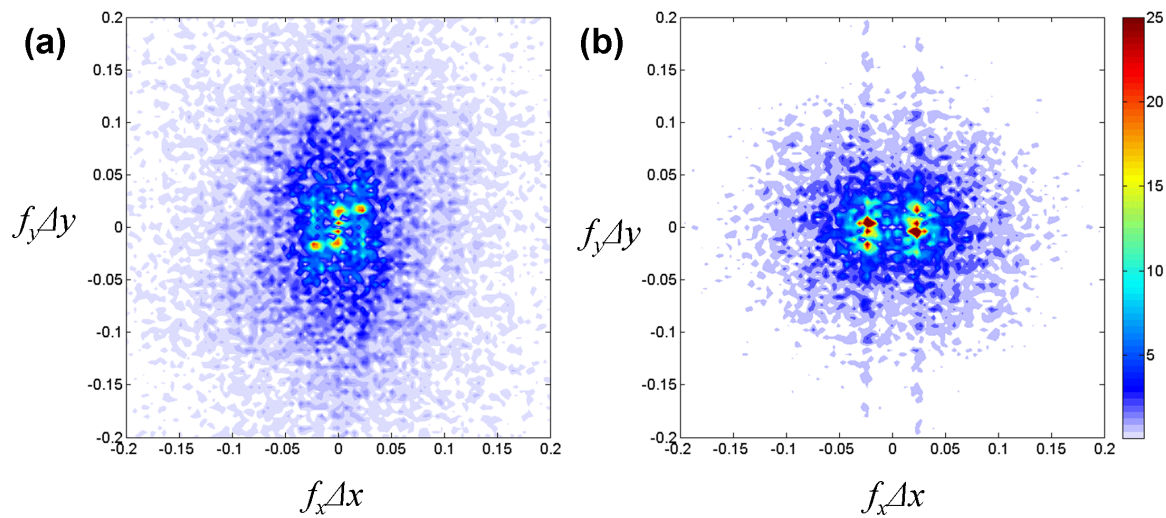
Subsequently, low-pass filtering was carried out by setting to zero all the Fourier coefficients below the desired cut-off characteristic length  $\lambda$ . The instantaneous low-pass filtered fluctuation velocity fields in the space domain were obtained by an inverse Fourier transform of the velocity data in the spatial-frequency domain. The high-pass filtered fluctuation velocity field for each instant was obtained by subtracting the low-pass filtered fluctuation velocity field and the ensemble-averaged velocity field from the instantaneous velocity field. Of course, the cut-off spatial-frequency or cut-off length  $\lambda$  is a critical parameter in the process of spatial filtering in order to separate the contribution of small-scale fluctuations from large-scale fluctuations. However, the determination of its value is rather arbitrary in this case and is partly limited by the spatial resolution of the velocity field from 2D PIV results.



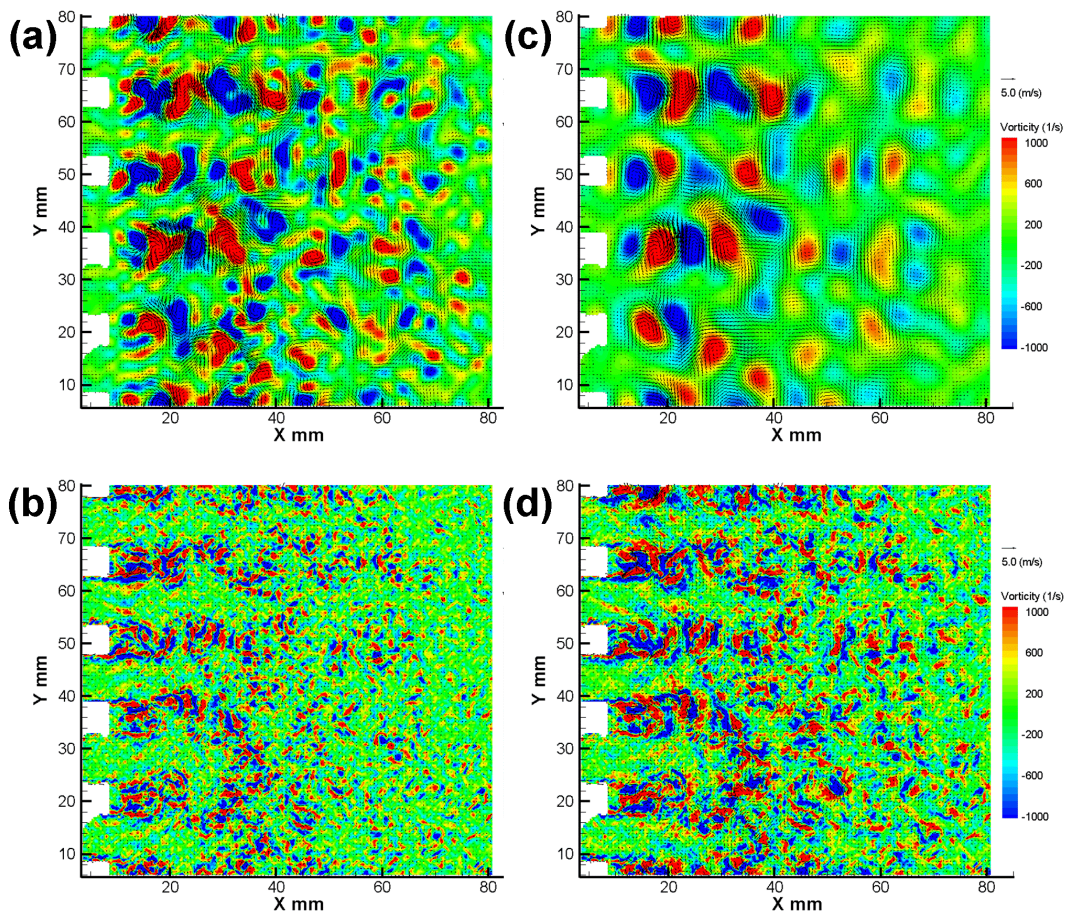
**Figure 15 Schematic of the spatial filtering algorithm based on 2D FFT, for separating instantaneous velocity fields according to the length-scales of eddies present in the flow**

Figure 17 (again based on the results shown in Figure 7c) shows the decomposition of an instantaneous velocity field into two parts: the large-scale velocity fluctuation field (top row) and the small-scale velocity fluctuation field (bottom row), based on the original ensemble average field shown in Figure 7d and the instantaneous field shown in 7c. The vorticity fields shown in Figure 17 are simply reconstructed using the fluctuation component of velocity to visualise the different vorticity scales. The cut-off length  $\lambda$  was set as 1.9 mm (left column) and 3.9 mm (right column) respectively. A substantial part of the flow structures formed at the plate ends is included in the large-scale fluctuations, and they are essentially different in strength, size and location from instant to instant, otherwise they would have been included in the ensemble-averaged flow field. The reconstructed vorticity field below the cut-off length scales reveals

randomly distributed small scale eddies that would be responsible for “small scale turbulence” as described in Section 4.4.



**Figure 16** 2D amplitude spectrum maps computed from the instantaneous fluctuation  $u'$  (a) and  $v'$  (b) using 2D spatial FFT,  $f_x \Delta x$  and  $f_y \Delta y$  being the spatial-frequency in respective directions. An arbitrary scale is used for comparisons.



**Figure 17** Velocity and vorticity fields obtained from spatial filtering of data shown in Figure 7c, using the cut-off length of 1.9 mm (a and b) and 3.9 mm (c and d). The top row shows large scale vortex structures obtained from instantaneous velocity fluctuation after low-pass filtering, while the bottom row corresponds to high-pass filtering. Stack II,  $Dr = 2.0\%$ , phase  $\Phi 8$ .

The distributions of the combined RMS value of large-scale fluctuation and small-scale fluctuation (turbulence intensity) are shown in Fig. 18 and Fig. 19 respectively, for the case of Stack II at  $D_r = 2.0\%$ , and the cut-off length chosen as 3.9 mm. The regions in the flow field affected by the large- and small-scale fluctuation are somewhat similar at each individual phase, although small-scale fluctuation tends to be stronger in an area closer to the plate end. It is interesting to see that the combined RMS value of large-scale fluctuation can reach about 50% of the mean velocity amplitude, while the combined RMS value of small-scale fluctuation is rarely more than 20% of the mean velocity amplitude. Compared with the distribution of the total fluctuation intensity shown by Fig. 11, the distribution of the combined RMS value of large-scale fluctuation reveals that it contributes a large part to the evaluated total fluctuation intensity at least at this test condition.

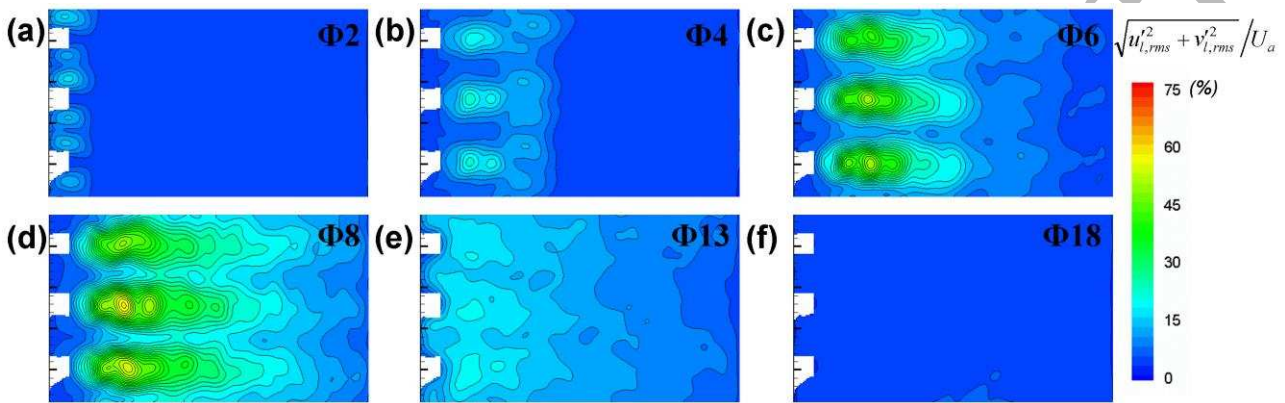


Figure 18 Distribution of the relative large-scale fluctuation; Stack II,  $D_r = 2.0\%$ ,  $\lambda = 3.9\text{mm}$

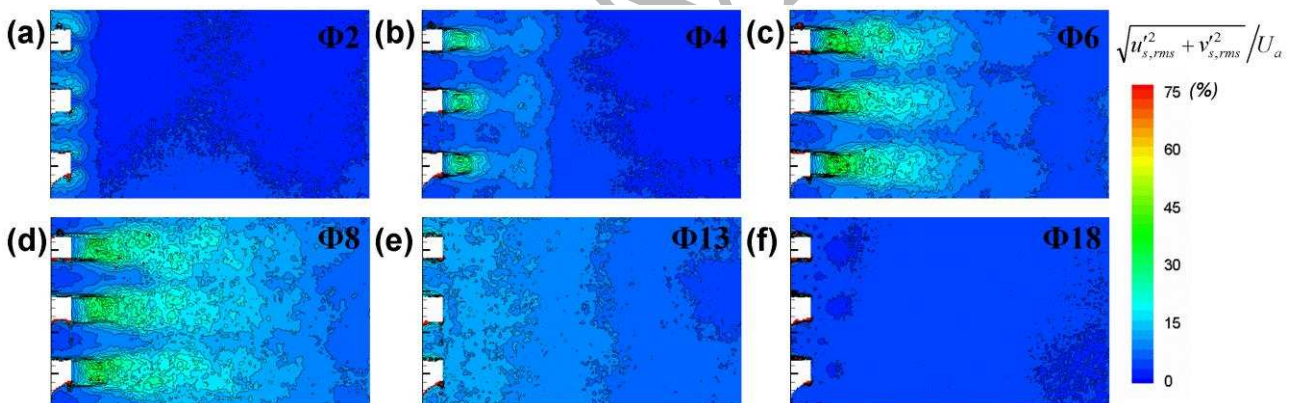


Figure 19 Distribution of the relative small-scale fluctuation; Stack II,  $D_r = 2.0\%$ ,  $\lambda = 3.9\text{mm}$

## 5 Conclusion and future work

This paper addresses the need for understanding turbulence characteristics of oscillatory flows past a stack of parallel plates. This particular configuration is important in the context of thermoacoustic engines and refrigerators, where an oscillatory flow is responsible for hydrodynamic energy transport along the stack, but also facilitates heat transfer between the stack and adjacent heat exchangers. The focus of this work is the development of PIV measurement techniques and methods of data processing and representation for characterisation of turbulent flows at the end of the parallel plate stack.

A typical focus of previous work was the flow pattern characterisation of the fluid motion out of the stack (i.e. ejection stage) based on the ensemble averaging of a large number of phase-locked PIV images. However, the presented

results indicate that such a description is relatively simplistic. The cycle-to-cycle variability of the flow field can be very significant, and to the authors' knowledge this aspect has not gained a sufficient recognition. Results presented in this paper show that it is possible to describe the unsteady/turbulent flow behaviour using classical Reynolds decomposition and subsequently analyse the fluctuation intensity "maps". Furthermore, it has been suggested that simplified parameters such as area-averaged or area-cycle-averaged turbulent kinetic energy can be used to compare the flow unsteadiness generated by different stack configurations and flow forcing. It is hoped that such data could help the modelling efforts on predicting the heat transfer rates between stacks and heat exchangers. However, in addition to the classical approach of calculating the fluctuation intensities a new methodology was proposed for spatial filtering of instantaneous fluctuation velocity fields in order to separate the contributions from large- and small-scale flow structures to the overall fluctuation intensity. It has been suggested that the term "turbulence intensity" should only be associated with the small scale vortex structures, which are more likely to control the heat transfer processes.

However, the work presented is only a first step in developing a deeper understanding of energy transfer processes in thermoacoustic systems. There are two clear shortcomings of current approach: Firstly, the configuration is simplified to enable the evaluation of measurement methodologies – in reality the stack will be coupled to a heat exchanger and so the flow field will be much more complicated, especially as the two structures would effectively be in each other's wakes. Secondly, the arrangement studied is isothermal, and so there is no opportunity to study the actual heat transfer processes. Therefore a further improvement would be to impose appropriate thermal boundary conditions on the structures studied and combine PIV with temperature field measurement, for example by Planar Laser Induced Fluorescence (PLIF). These will be the directions of future experimental work. Finally, based on such experimental results, significant research effort is needed on performing similarity analysis on a wide range of geometrical configurations to formulate criterial equations describing the energy transfer mechanisms.

## Acknowledgments:

The authors wish to thank the Engineering and Physical Sciences Research Council UK for supporting this work under grants: GR/S26842/01, GR/T04502/01 (EPSRC Advanced Research Fellowship), GR/T04519/01 and EP/E044379/1.

## References:

- [1] Swift G W, 1988, Thermoacoustic engines, *J. Acoust. Soc. Am.*, 84(4), 1145-1180
- [2] Yazaki T, Iwata A, Maekawa T & Tominaga A 1998 Traveling wave thermoacoustic engine in a looped tube, *Phys. Rev. Lett.*, 81(15), 3128-3131
- [3] Rott N, 1980, Thermoacoustics, *Adv. Appl. Mech.*, 20, 135-175
- [4] Adrian R J, 2005, Twenty years of particle image velocimetry, *Exp. Fluids*, 39, 159-169
- [5] Schroeder A, Willert C E (eds.), 2008, *Particle Image Velocimetry - New Developments and Recent Applications*, Springer-Verlag, Berlin, Heidelberg
- [6] Kompenhans J, Tropea C, 1997, Editorial, *Meas. Sci. Technol.*, 8, doi: 10.1088/0957-0233/8/12/001
- [7] Trinité M and Lecordier B, 2001, Editorial, *Meas. Sci. Technol.*, 12, doi: 10.1088/0957-0233/12/9/001
- [8] Tropea C, 2002, Editorial, *Meas. Sci. Technol.*, 13, doi: 10.1088/0957-0233/13/7/001
- [9] Hinsch K D and Herrmann S F, 2004, Holographic particle image velocimetry (Editorial), *Meas. Sci. Technol.*, 15(4), doi: 10.1088/0957-0233/15/4/E01
- [10] Sung H J, Kim K C and Lee S J, 2004, 5th International Symposium on Particle Image Velocimetry, PIV'03 (Editorial), *Meas. Sci. Technol.*, 15(6), doi: 10.1088/0957-0233/15/6/E01
- [11] Okamoto K, 2006, 6th International Symposium on Particle Image Velocimetry 2005 (Editorial), *Meas. Sci. Technol.*, 17(7), doi: 10.1088/0957-0233/17/7/E01
- [12] Guibert P and Lemoyne L, 2002, Dual particle image velocimetry for transient flow field measurements: Autocorrelation estimation of in-cylinder flow of a spark ignition engine turbulence, *Experiments in Fluids*, 33, 355-367
- [13] Bevan K E and Ghandhi J B, 2008, Particle Image Velocimetry Measurements of In-Cylinder Flow in a Four-Stroke Utility Engine and Correlation with Combustion Measurements, *Journal of Engineering for Gas Turbines and Power*, 130, 032802-1-11

- [14] Reuss D L, Megerle M and Sick V, 2002, Particle-image velocimetry measurement errors when imaging through a transparent engine cylinder, *Meas. Sci. Technol.*, 17, 1029-1035
- [15] Hann D B and Greated C A, 1997, Particle image velocimetry for the measurement of mean and acoustic particle velocities, *Meas. Sci. Technol.*, 8, 656-660
- [16] Hann D B and Greated C A, 1997, The measurement of flow velocity and acoustic particle velocity using particle-image velocimetry, *Meas. Sci. Technol.*, 8, 1517-1522
- [17] Campbell M, Cosgrove J A, Greated C A, Jack S and Rockliff D, 2000, Review of LDA and PIV applied to the measurement of sound and acoustic streaming, *Optics and Laser Technology*, 32, 629-639
- [18] Nabavi M, Siddiqui M H K and Dargahi J, 2007, Simultaneous measurement of acoustic and streaming velocities using synchronized PIV technique, *Meas. Sci. Technol.*, 18, 1811-1817
- [19] Debesse Ph, Baltean-Carlès D, Lusseyran F and François M-X, 2008, Experimental analysis of nonlinear phenomena in a thermoacoustic system, *AIP Conference Proceedings*, 1022, 355-358
- [20] Blanc-Benon P, Besnoin E and Knio O M, 2003, Experimental and computational visualization of the flow in a thermoacoustic stack, *C R. Mécanique*, 331, 17-24
- [21] Castrejón-Pita J R, Castrejón-Pita A A, Huelisz G, Tovar R, 2006, Experimental demonstration of the Rayleigh acoustic viscous boundary layer theory, *Physical Review E*, 73(3), 036601
- [22] Berson A and Blanc-Benon Ph, 2007, Nonperiodicity of the flow within the gap of a thermoacoustic couple at high amplitudes, *J. Acoust. Soc. Am.*, 122(4), EL122-EL127
- [23] Berson A, Michard M and Blanc-Benon Ph, 2008, Measurement of acoustic velocity in the stack of a thermoacoustic refrigerator using particle image velocimetry, *Heat Mass Transfer*, 44, 1015-1023
- [24] Mao X, Yu Z, Jaworski A J, Marx D, 2008, PIV studies of coherent structures generated at the end of a stack of parallel plates in a standing wave acoustic field, *Exp. Fluids*, 45, 833-846
- [25] Aben P C H, Bloemen P R and Zeegers J C H, 2009, 2-D PIV measurements of oscillatory flow around parallel plates, *Exp. Fluids*, 46, 631-641
- [26] Jaworski A J, Mao X, Mao X, Yu Z, 2009, Entrance effects in the channels of the parallel plate stack in oscillatory flow conditions, *Experimental Thermal and Fluid Science*, 33, 495-502
- [27] Worlikar A S and Knio O M, 1996, Numerical simulation of a thermoacoustic refrigerator – Part I: Unsteady adiabatic flow around the stack, *Journal of Computational Physics*, 127, 424-451
- [28] Worlikar A S, Knio O M and Klein R, 1998, Numerical simulation of a thermoacoustic refrigerator – Part II: Stratified flow around the stack, *Journal of Computational Physics*, 144, 299-324
- [29] Besnoin E and Knio O M, 2004, Numerical study of thermoacoustic heat exchangers, *Acta Acustica United with Acustica*, 90, 432-444
- [30] Marx D and Blanc-Benon Ph, 2004, Computation of the mean velocity field above a stack plate in a thermoacoustic refrigerator, *Comptes Rendus Mécanique*, 332, 867-874
- [31] Marx D, Mao X and Jaworski A J, 2006, Acoustic coupling between the loudspeaker and the resonator in a standing-wave thermoacoustic device, *Applied Acoustics*, 67, 402-419
- [32] Keane R D and Adrian R J, 1990, Optimization of particle image velocimeters. Part I: Double pulsed systems, *Measurement Science and Technology*, 1, 1202-1215
- [33] Melling A, 1997, Tracer particles and seeding for particle image velocimetry, *Meas. Sci. Technol.*, 8, 1406-1416
- [34] King L V, 1934, On the acoustic radiation pressure on spheres, *Proceedings of the Royal Society of London, A*, 147, 212-240
- [35] Raffel M, Willert C E, Wereley S T and Kompenhans J, 2007, *Particle Image Velocimetry, A Practical Guide*, Second Edition, Springer
- [36] Keane R D and Adrian R J, 1991, Optimization of particle image velocimeters: II. Multiple pulsed systems, *Meas. Sci. Technol.*, 2, 963-974
- [37] Hart D P, 1999, Super-resolution PIV by recursive local-correlation, *Journal of Visualization*, 3(2), 187-194
- [38] Zimmerman W B, 2002, The drag on sedimenting discs in broadside motion in tubes, *International Journal of Engineering Science*, 40, 7-22
- [39] Zimmerman W B, 2004, On the resistance of a spherical particle settling in a tube of viscous fluid, *International Journal of Engineering Science*, 42, 1753-1778
- [40] Womersley J. R., 1955, Method for the calculation of velocity, rate of flow and viscous drag in arteries when the pressure gradient is known, *Journal of Physiology*, 127, 553-563
- [41] Arnott W. P., 1991, General formulation of thermoacoustics for stack having arbitrarily shaped pore cross sections, *Journal of Acoustical Society of America*, 90(6), 3228-3237
- [42] Hino M, Kashiwayanagi M, Nakayama A, Hara T, 1983, Experiments on the turbulence statistics and the structure of a reciprocating oscillatory flow, *Journal of Fluid Mechanics*, 131, 363-400
- [43] Hyun B S, Balachandar R, Yu K and Patel V C, 2003, Assessment of PIV to measure mean velocity and turbulence in open-channel flow, *Experiments in Fluids*, 35, 262-267
- [44] Cenedese A, Doglia G, Romano G P, Michele G De and Tanzini G, 1994, LDA and PIV velocity measurements in free jets, *Experimental Thermal and Fluid Science*, 9, 125-134
- [45] Regunath G S, Zimmerman W B, Tesaf V and Hewakandamby B N, 2008, Experimental investigation of helicity in turbulent swirling jet using dual-plane dye laser PIV technique, *Experiments in Fluids*, 45, 973-986
- [46] Pai S-I, 1957, *Viscous flow theory, II – Turbulent flow*, D. van Nostrand Company, Inc.
- [47] Nelson M A, Brown M J, Pardyjak E R and Klewicki J C, 2004, Area-averaged profiles over the mock urban setting test array, *Proc. 5<sup>th</sup> Symposium on the Urban Environment*, 577-581, August 23-26

- [48] Nelson M A, Pardyjak E R, Klewicki J C, Pol S U and Brown M J, 2007, Properties of the Wind Field within the Oklahoma City Park Avenue Street Canyon. Part I: Mean Flow and Turbulence Statistics, *Journal of Applied Meteorology and Climatology*, 46, 2038-2054
- [49] Lowery G W and Vachon R I, 1975, The effect of turbulence on heat transfer from heated cylinders, *Int. J. Heat Mass Transfer*, 18, 1229-1242
- [50] Kondjoyan A and Daudin J D, 1995, Effects of free stream turbulence intensity on heat and mass transfers at the surface of a circular cylinder and an elliptical cylinder, axis ratio 4, *Int. J. Heat Mass Transfer*, 38(10), 1735-1749
- [51] Lavender W J and Pei D C T, 1967, The effect of fluid turbulence on the rate of heat transfer from spheres, *Int. J. Heat Mass Transfer*, 10, 529-539
- [52] Peyrin F and Kondjoyan A, 2002, Effect of turbulent integral length scale on heat transfer around a circular cylinder placed cross to an air flow, *Experimental Thermal and Fluid Science*, 26, 455-460
- [53] Sak C, Liu R, Ting D S-K and Rankin G W, 2007, The role of turbulence length scale and turbulence intensity on forced convection from a heated horizontal circular cylinder, *Experimental Thermal and Fluid Science*, 31, 279-289
- [54] Piirto M, Ihalainen H, Eloranta H and Saarenrinne P, 2001, 2D Spectral and Turbulence Length Scale Estimation with PIV, *Journal of Visualisation*, 4, 39-49

Advanced Manuscript